A Comparative Analysis of Key Performance Indicators for RIS-Enhanced Non-Terrestrial and Terrestrial Localization

Alda Xhafa, Daniel Egea-Roca, José A. López-Salcedo, and Gonzalo Seco-Granados

***Abstract*—Reconfigurable Intelligent Surface (RIS) offers a promising solution for improving localization in complex environments by enhancing signal coverage and accuracy. RISs can reflect signals to obstructed areas, making them valuable for Terrestial Network (TN)s. While Non-Terrestial Network (NTN)s, such as Low Earth Orbit (LEO) satellite constellations, offer global coverage and high data rates, they face challenges like high path loss and Doppler shifts that hinder localization. This paper compares RIS-aided localization in TN and NTN environments, evaluating performance metrics such as accuracy, coverage, and mobility support through simulations. A custom-built simulator is used to perform the analysis, allowing to assess the trade-offs of RIS deployment. The results provide insights into optimizing RIS-enhanced localization systems for future networks, highlighting the benefits and limitations for both TN and NTN scenarios.**

***Index Terms*—Reconfigurable intelligent surface, KPI, TN and NTN systems, coverage, dynamic range.**

I. Introduction

The evolution of 5G localization systems [1]–[3] has reached a pivotal stage, driven by the need for ubiquitous, high-precision positioning across diverse environments. Traditional TNs [4] rely on infrastructure such as base stations (BSs) to estimate User Terminals (UTs) through time of arrival (ToA), and/or Angle of Departure (AoD). However, these methods suffer in non-line-of-sight (NLoS) and indoor environments due to signal blockage and multipath interference [5], [6]. Conversely, NTNs [7], particularly LEO satellite constellations, offer global coverage but face challenges such as atmospheric attenuation, Doppler shifts, and ionospheric delays which degrade positioning accuracy. To address these limitations, RISs have emerged as a transformative technology, reshaping signal propagation in both TN and NTN scenarios [8]–[10]. In TNs [11], [12], RISs functions as programmable reflectors that create virtual anchors, improving geometric diversity for localization. Far-field RISs configurations have demonstrated sub-meter positioning accuracy in 5G networks by exploiting channel state information and Fisher Information Matrix (FIM) analysis [13]. In NTNs [8], [14], RISs can mitigate path loss and compensate for Doppler effects by dynamically steering signals toward obscured UTs. More importantly, RISs provide additional anchor points for localization, enabling accurate positioning with a single LEO satellite, an essential advantage given the limited visibility of LEO satellites, where in some cases, only one satellite may be available at a time. Recent studies have demonstrated improved Position Error Bound (PEB) through optimized phase profile design [15]. Despite these advances, a comprehensive comparison of RIS benefits in TNs versus NTNs remains limited, particularly in terms of accuracy, coverage, and dynamic range. Moreover, a rigorous analysis of NTN scenarios is still lacking, as most existing studies assume satellite positions with zero Doppler, overlooking the impact of realistic orbital dynamics [14].

This paper aims to fill this gap by addressing three key challenges. First, while RIS-aided TN localization has been extensively studied in terms of channel modeling and resource allocation [4], NTN implementations remain underexplored due to factors like orbital dynamics. Second, integrating TN and NTN requires unified performance metrics for evaluating localization systems. Third, existing Key Performance Indicators (KPI)s for RIS-based localization, such as PEB and root mean square error (RMSE), often neglect NTN-specific impairments like high Doppler shifts. To address these challenges, we propose a RIS-aided localization simulation framework for both TN and NTN scenarios, incorporating realistic channel impairments, mobility effects, and far-field modeling, while accounting for time-varying factors such as delays, satellite positions (Angle of Arrival (AoA)), and signal gains. The framework supports various Orthogonal Frequency Division Multiplexing (OFDM) configurations, including flexible subcarrier spacing, bandwidth, transmission power, and RIS sizes. Furthermore, we conduct a KPI-based comparative analysis of TN and NTN localization, evaluating positioning accuracy, coverage, and dynamic range under different configurations, including random and directional RIS phase profiles. Our approach enables a comprehensive performance evaluation through key metrics such as PEB, cumulative density function (cdf), carrier-to-noise ratio (CN0), symbol count and RIS size. It provides the first detailed evaluation of RIS-aided localization in NTN, and a direct comparison to TN.

The paper is structured as follows: Sec. II describes the scenario for the simulations; Sec. III presents the signal model and the details on channel parameters and position estimations; Sec. IV describes the KPI parameters and outlies the evaluation results; Sec. V draws the conclusions.

II. System model

We consider a far-field, narrow-band cmWave system comprising a single-antenna transmitter, a single antenna receiver UT, and a single RIS composed of a Uniform Rectangular Array (URA). Both TN and NTN scenarios are addressed, differing in the transmitter: a BS in TN, and a LEO satellite in NTN.

A. Scenario geometry

In both cases, the RIS is located at a known location $\boldsymbol{p}_{\text{RIS}} = [x_{\text{RIS}}, y_{\text{RIS}}, z_{\text{RIS}}]^\top$, with known orientation defined by Euler angles $\boldsymbol{o} = [\alpha, \beta, \gamma]^\top$. In this work, RIS is placed at the origin of the global coordinate frame (GCF) in the vicinity of UT. RIS is equipped with a URA of $M = M_r \times M_c$ elements, where M_r and M_c are the number of elements placed along its local x and z-axes respectively. The position of its element is located at $\mathbf{q}_m \in \mathbb{R}^3$ in the local coordinate frame (LCF)

A. Xhafa, D. Egea-Roca, J. A. López-Salcedo, G. Seco-Granados are with Dept. of Telecommunication and Systems Engineering IEEC-CERES, UAB, Spain (e-mail: alda.xhafa@uab.cat; daniel.egea@uab.cat; jose.salcedo@uab.cat; gonzalo.seco@uab.cat).

This work was founded by the European Union under the HE-ESA-005 activity. Views and opinions expressed are, however, those of the author(s) only and the European Commission and/or EUSPA and/or ESA cannot be held responsible for any use which may be made of the information contained therein. This work has also been partly supported by the Catalan government in the framework of the Catalan New Space Strategy and the AGAUR-ICREA Academia Program, and by the Spanish Agency of Research (AEI) under grant PID2023-152820OB-I00 funded by MICIU/AEI/10.13039/501100011033 and the ERDF/EU.

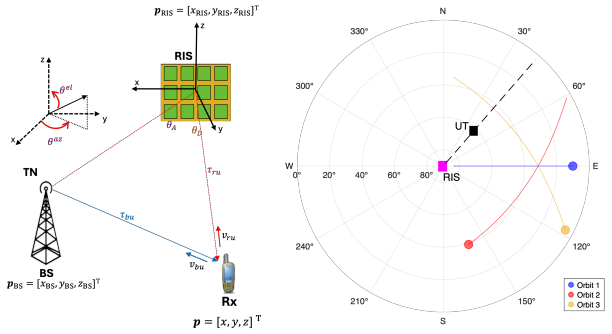

Fig. 1. Illustration of the system model: (left) TN case together with the representation of azimuth θ^{az} and elevation angle θ^{el}, NTN case is similar, but with a satellite replacing the BS, (right) NTN scenario showing RIS in purple, the UT in black, and the three satellite orbits considered.

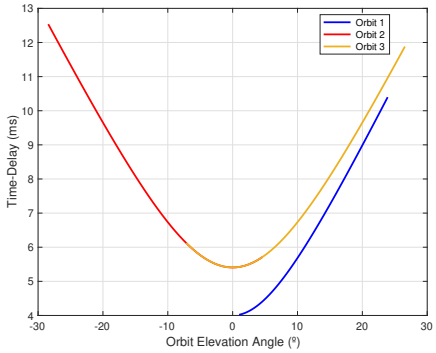

Fig. 2. Propagation time (delay) of the LoS path in an NTN scenario for three satellite orbits.

spaced by $d = \lambda/2$, where $\lambda = c/f_c$ is the wavelength, f_c is the carrier frequency, and c is the speed of light. Thus, $\mathbf{q}_m = \{d\left(\lfloor m/M_c \rfloor - (M_r-1)/2\right),\ 0,\ d\left((m \bmod M_c) - (M_c-1)/2\right)\}$. The UT moves with unknown velocity $\boldsymbol{v} \in \mathbb{R}^3$ and unknown position $\boldsymbol{p} \in \mathbb{R}^3$. The system is asynchronous with an unknown but fixed clock bias between the transmitter and UT.

In TN, the BS is located at a known location $\boldsymbol{p}_{\text{BS}} \in \mathbb{R}^3$ and it is assumed static (see Fig. 1 (left side)). In NTN, the satellite in a LEO orbit. The state of the satellite: position $\boldsymbol{p}_{\text{sat}} \in \mathbb{R}^3$, and velocity $\boldsymbol{v}_{\text{sat}} \in \mathbb{R}^3$ determined by the orbit dynamic defined by Keplerian parameters [16] $\{h, \theta_{\text{I}}, \theta_{\text{AN}}, \theta_{\text{PG}}, \psi\}$: orbit height, inclination, ascending node angle, perigee angle, and elevation angle respectively. The first four define the orbit plane in the GCF, and ψ describes the satellite's position in the orbit LCF. Three different orbits are considered: Orbit 1 with $\theta_{\text{I}} = 90°$ and $\theta_{\text{AN}} = -90°$, Orbit 2 and Orbit 3 with $\theta_{\text{I}} = 81°$ and $\theta_{\text{AN}} = \pm 45°$, respectively. All with $\theta_{\text{PG}} = 90°$. Regarding the orbit trajectory, let $R_{\text{c}} = R_{\text{E}} + h$ be the constellation radius with R_{E} the Earth radius. Then, for a given (orbit) elevation angle at time t, ψ_t, we have the following satellite state:

$$\begin{aligned} \tilde{\boldsymbol{p}}_{\text{sat}}^{(t)} &= R_{\text{c}}[\cos(\psi_t), \sin(\psi_t), 0]^\top, \\ \tilde{\boldsymbol{v}}_{\text{sat}}^{(t)} &= v_{\text{sat}}[-\sin(\psi_t), \cos(\psi_t), 0]^\top, \end{aligned} \tag{1}$$

where $v_{\text{sat}} = \omega_{\text{m}} R_{\text{c}}$, and $\omega_{\text{m}} = \sqrt{F_{\text{m}}/R_{\text{c}}^3}$ with $F_{\text{m}} = 4.0038 \cdot 10^{14}$ m^3/s^2. The model can be updated every time interval $T > 0$ by $\tilde{\boldsymbol{p}}_{\text{sat}}(t+T) = \tilde{\boldsymbol{p}}_{\text{sat}}(t) + \tilde{\boldsymbol{v}}_{\text{sat}}(t)T$. Note that $\psi_t = \arctan([\tilde{\boldsymbol{p}}_{\text{sat}}]_2/[\tilde{\boldsymbol{p}}_{\text{sat}}]_1)$, which can be used in (1) to update the satellite velocity. These coordinates are in the orbit LCF, and to obtain GCF, a known rotation is required first followed by a translation of R_{E} in the z-axis [16]: $\mathbf{p}_{\text{sat}}(t) = \boldsymbol{R}_{\text{sat}}\tilde{\mathbf{p}}_{\text{sat}}(t) - [0,\ 0,\ R_{\text{E}}]^\top$, with $\boldsymbol{R}_{\text{sat}}$ being the rotation matrix. The setting of the NTN scenario is shown in the sky-plot of Fig. 1 (the right side) centered at the origin of the GCF. It allows us to describe the orbit trajectories with $\boldsymbol{p}_{\text{sat}}^{(t)}$ and to analyze the variation in propagation time or time delay as shown in Fig. 2 for $h = 1200$ km and the three considered orbits.

B. Direct and reflected channel paths

The channel parameters of the proposed system are based on two channel paths: the direct path between the transmitter Tx and the UT denoted with the subscript "tu" (i.e., t=(b,s) when Tx is a BS in TN or a satellite in NTN respectively); the reflection path between the transmitter, RIS and UT, also considered as the RIS path, denoted with the subscript "ru".

1) Direct channel path: The channel parameters of direct path include channel delay τ_d, and Doppler frequency shift f_d. The time delay is expressed as $\tau_d = \|\boldsymbol{p}_{\text{tx}} - \boldsymbol{p}\|/c + \delta t$, where δt is the unknown fixed clock bias between Tx (BS or LEO satellite and UT), $\boldsymbol{p}_{\text{tx}}$ is the $\boldsymbol{p}_{\text{BS}} \in \mathbb{R}^3$ or $\boldsymbol{p}_{\text{sat}} \in \mathbb{R}^3$, and $\boldsymbol{p} \in \mathbb{R}^3$ is the location of UT, all in GCF. The Doppler shift $f_0 = [(\boldsymbol{v}_{\text{tx}} - \boldsymbol{v})^\top(\boldsymbol{p} - \boldsymbol{p}_{\text{tx}})]/(\lambda\|\boldsymbol{p} - \boldsymbol{p}_{\text{tx}}\|)$. Note that, in NTN $\boldsymbol{v}_{\text{tx}} \neq \mathbf{0}$ due to satellite motion, while in TN, the BS is assumed static, i.e., $\boldsymbol{v}_{\text{tx}} = \mathbf{0}$. Therefore, the Doppler shift in TN is simplified in $f_0^{\text{TN}} = [-\boldsymbol{v}^\top(\boldsymbol{p} - \boldsymbol{p}_{\text{BS}})]/(\lambda\|\boldsymbol{p} - \boldsymbol{p}_{\text{BS}}\|)$. The radial velocity is $v_0 = f_0/f_c$.

2) Reflection channel path: This path, known also as the RIS path, includes the channel path between Tx and RIS, and the channel path between RIS and UT. The time delay and doppler shift of the RIS path is defined as:

$$\tau_r \doteq \tau_{\text{tr}} + \tau_{\text{ru}} = \frac{\|\boldsymbol{p}_{\text{Tx}} - \boldsymbol{p}_{\text{RIS}}\| + \|\boldsymbol{p}_{\text{RIS}} - \boldsymbol{p}\|}{c} + \delta t, \tag{2}$$

$$f_r \doteq f_{\text{tr}} + f_{\text{ru}} = \frac{\boldsymbol{v}_{\text{Tx}}^\top(\boldsymbol{p}_{\text{Tx}} - \boldsymbol{p}_{\text{RIS}})}{\lambda\|\boldsymbol{p}_{\text{Tx}} - \boldsymbol{p}_{\text{RIS}}\|} + \frac{\boldsymbol{v}^\top(\boldsymbol{p}_{\text{RIS}} - \boldsymbol{p})}{\lambda\|\boldsymbol{p}_{\text{RIS}} - \boldsymbol{p}\|}. \tag{3}$$

Since in TN the BS is assumed static, $f_{\text{tr}} = 0$, and therefore the (3) in TN is simplified in $f_r^{\text{TN}} = [\boldsymbol{v}^\top(\boldsymbol{p}_{\text{RIS}} - \boldsymbol{p})]/(\lambda\|\boldsymbol{p}_{\text{RIS}} - \boldsymbol{p}\|)$. The radial velocity is $v_r = f_r/f_c$. In addition, the AoA and AoD observed at and from RIS, collectively denoted by the subscript $g \in \{\text{A}, \text{D}\}$, are characterized by their azimuth and elevation components respectively $\boldsymbol{\theta}_{\text{g}} = [\phi_{\text{g}}, \theta_{\text{g}}]^\top$. Given a vector $\Delta\boldsymbol{p}_g = \boldsymbol{p}_g - \boldsymbol{p}_{\text{RIS}}$, where $\boldsymbol{p}_g \in \{\boldsymbol{p}_{\text{tx}}, \boldsymbol{p}\}$ represents the position of Tx or UT in GCF. The angles are computed in the LCF using the rotation matrix $\boldsymbol{R}$ as: $\phi_g = \arctan 2\left(\left[\boldsymbol{R}^\top\Delta\boldsymbol{p}_g\right]_2, \left[\boldsymbol{R}^\top\Delta\boldsymbol{p}_g\right]_1\right)$ and $\theta_g = \arccos\left(\left[\boldsymbol{R}^\top\Delta\boldsymbol{p}_g\right]_3/\|\Delta\boldsymbol{p}_g\|\right)$, with ϕ_g and θ_g being the azimuth and elevation angles, respectively as in Fig. 1.

III. Signal Model and Receiver Processing

In this section, details about signal model, channel parameters, and position estimation are described.

A. Signal model

This paper considers the transmission of an OFDM signal with N subcarriers and L symbols. The total symbol duration is given by $T_{\text{sym}} = T + T_{\text{CP}}$, where $T = 1/\Delta f$ is the useful symbol duration, T_{CP} is the Cycle Prefix (CP) duration, and $\Delta f = B/N$ denotes the subcarrier spacing, with B being the total signal bandwidth. The total transmit power P_{tot} is uniformly distributed across the subcarriers,

resulting in a per-subcarrier power of $P_{\mathrm{s}} = P_{\mathrm{tot}}/N$. The complex baseband signal $s^l(t)$ for the l-th transmitted symbol is given by:

$$s^l(t) = \sqrt{P_{\mathrm{s}}} \sum_{k=0}^{N-1} x_{k,l} e^{j2\pi k \Delta f (t - lT_{\mathrm{sym}})} g(t - lT_{\mathrm{sym}}), \quad (4)$$

where $x_{k,l} \in \mathbb{C}$ denotes the pilot symbol transmitted on the k-th subarrier during l-th symbol, and $g(t) = 1$ for $t \in [0, T_{\mathrm{sym}}]$, and 0 otherwise. Then, the transmitted passband signal is $\tilde{s}^l(t) = \mathbb{R}\left\{s^l(t) e^{j2\pi f_c t}\right\}$.

The received baseband signal comes from the direct LoS path and the RIS path. After downconversion and sampling at $t = lT_{\mathrm{sym}} + T_{\mathrm{CP}} + \kappa T/N$, where $\kappa = 0, 1, \ldots, K-1$, the sampled version of the received signal is $\tilde{y}^l[\kappa] = \tilde{y}^l_{\mathrm{LoS}}[\kappa] + \tilde{y}^l_{\mathrm{RIS}}[\kappa] + n^l[\kappa]$, with $n^l[\kappa]$ being the thermal noise with power spectral density (PSD) N_0. The discrete-time signal of each path for the l-symbol can be expressed as [17]:

$$\begin{aligned}
\tilde{y}^l_{\mathrm{LoS}}[\kappa] &= \sqrt{P_s}\alpha_d \, e^{j2\pi f_d \frac{\kappa T}{N}} \sum_{k=0}^{N-1} x_{k,l} \, e^{j2\pi \frac{k\kappa}{N}} \\
&\quad \times e^{j2\pi f_d l T_{\mathrm{sym}}} e^{-j2\pi k \Delta f (\tau_d - \upsilon_d l T_{\mathrm{sym}})}, \\
\tilde{y}^l_{\mathrm{RIS}}[\kappa] &= \sqrt{P_s}\alpha_r G_l(\boldsymbol{\theta}) \, e^{j2\pi f_r \frac{\kappa T}{N}} \sum_{k=0}^{N-1} x_{k,l} \, e^{j2\pi \frac{k\kappa}{N}} \\
&\quad \times e^{j2\pi f_r l T_{\mathrm{sym}}} e^{-j2\pi k \Delta f (\tau_r - \upsilon_r l T_{\mathrm{sym}})}, \quad (5)
\end{aligned}$$

where α_i, τ_i, f_i denote the channel amplitude, time delay, Doppler shift respectively of the i-th path ($i = d$ for the LoS path and $i = r$ for the RIS path), and $\boldsymbol{\theta} = [\boldsymbol{\theta_A}, \boldsymbol{\theta_D}]$ the angle parameters AoA/AoD. The $G_l(\boldsymbol{\theta}) \in \mathbb{C}$ is the RIS beamforming gain expressed as:

$$G_l = \left[\boldsymbol{a}(\boldsymbol{\theta_A}) \odot \boldsymbol{a}(\boldsymbol{\theta_D})\right]^\top \boldsymbol{\Omega_l} = \sum_{m=1}^{M} e^{j\mathbf{u}(\theta_{\mathbf{A}})^\top \mathbf{q}_m} \left[\boldsymbol{\Omega_l}\right]_m e^{j\mathbf{u}(\theta_{\mathbf{D}})^\top \mathbf{q}_m}.$$

The vector $\boldsymbol{a}(\boldsymbol{\theta_i}) \in \mathbb{C}$ ($\mathbf{i} = \mathbf{A}, \mathbf{D}$) is the RIS's steering vector modeled by AoA and AoD for the angle $\boldsymbol{\theta_i} = (\theta_i^{\mathrm{az}}, \theta_i^{\mathrm{el}})$ and whose elements are $[\boldsymbol{a}(\boldsymbol{\theta_i})]_m = e^{j\boldsymbol{u}(\boldsymbol{\theta_i})^\top \boldsymbol{q}_m}$, where $\boldsymbol{u}(\boldsymbol{\theta_i}) = (2\pi/\lambda)[\sin(\theta_i^{\mathrm{el}})\cos(\theta_i^{\mathrm{az}}), \sin(\theta_i^{\mathrm{el}})\sin(\theta_i^{\mathrm{az}}), \cos(\theta_i^{\mathrm{el}})]^\top$ is the direction vector in LCF of the RIS corresponding to angle $\boldsymbol{\theta_i}$ and $\boldsymbol{q}_m$ is the position of the m-RIS element compared to the RIS center (see Sec. II). The $\boldsymbol{\Omega_l} = [e^{j\Omega_{l,1}}, \ldots, e^{j\Omega_{l,M}}]$ is the RIS phase profile vector (random or directional) at the l-th symbol [18]. For the random RIS profile, the phase shifts are randomly generated from a uniform distribution in $[0, 2\pi)$ generated for each RIS element. The directional phase profile is designed when an approximate UT position is known, by steering beams toward selected virtual targets within a sphere of radius σ as in [18].

In NTN, the channel parameters are time-varying due to satellite motion. As a result, each sample of an OFDM symbol may experience different Doppler shifts, path delays, AoA/AoD, and RIS phase profiles. However, we will assume operating conditions in which these parameters remain constant over the N samples of an individual OFDM symbol, but may vary across different OFDM symbols. This assumption should be reflected in (6) with an explicit dependence on l of α_i, τ_i, f_i, ..., however it has been omitted to simplify the notation. In contrast, for the TN scenario, the receiver signal model can be simplified to a time-invariant form since mobility is limited compared to NTN scenarios and delays are considered quasi-static during the observation window, therefore the channel parameters will be considered constant over time. Note that in the following signal model explanation, the NTN case will be considered and when applicable will be highlighted the assumptions from TN positioning to be neglected. By applying the FFT across the K samples of each symbol to enable subcarrier-wise processing, the frequency-domain received signal is given by $\tilde{\boldsymbol{Y}} = \tilde{\boldsymbol{Y}}_{\mathrm{LoS}} + \tilde{\boldsymbol{Y}}_{\mathrm{RIS}} + \boldsymbol{N}$, with $\boldsymbol{N} \in \mathbb{C}^{N,L}$ capturing the noise effect. The LoS and RIS terms are given by:

$$\begin{aligned}
\tilde{\boldsymbol{Y}}_{\mathrm{LoS}} &= \boldsymbol{A}_d \boldsymbol{F} \boldsymbol{E}(\boldsymbol{f}_d) \boldsymbol{F}^{\mathrm{H}} (\boldsymbol{C}(\boldsymbol{f}_d) \odot \boldsymbol{D}(\boldsymbol{\tau}_d) \odot \boldsymbol{X}), \\
\tilde{\boldsymbol{Y}}_{\mathrm{RIS}} &= \boldsymbol{A}_r \boldsymbol{F} \boldsymbol{E}(\boldsymbol{f}_r) \boldsymbol{F}^{\mathrm{H}} (\boldsymbol{C}(\boldsymbol{f}_r) \odot \boldsymbol{D}(\boldsymbol{\tau}_r) \odot \boldsymbol{G}(\boldsymbol{\theta}) \odot \boldsymbol{X}),
\end{aligned} \quad (6)$$

where $\boldsymbol{A}_i$ encapsulates the signal power and attenuation (constant in TN), and $\boldsymbol{F} \in \mathbb{C}^{N \times N}$ is the unitary DFT matrix with elements $F_{p,q} = 1/\sqrt{N} \exp\big(-j2\pi pq/N\big)$, for $p, q = 0, \ldots, N-1$. The Doppler-shift matrix is $[\boldsymbol{E}(\boldsymbol{f}_i)]_{k,k} = \exp\big(j2\pi f_i k T/N\big)$, while mobility induces a per-symbol phase evolution given by $[\boldsymbol{C}(\boldsymbol{f}_i)]_{k,l} = \exp\big(j2\pi f_i l T_{\mathrm{sym}}\big)$. The delay matrix is $[\boldsymbol{D}(\boldsymbol{\tau}_i)]_{k,l} = \exp\big(-j2\pi \Delta f \, k \, (\tau_i - \upsilon_i l T_{\mathrm{sym}})\big)$; in NTN the drift term $\upsilon_i l T_{\mathrm{sym}}$ may be significant, whereas in TN it can be neglected. Finally, $\boldsymbol{X} \in \mathbb{C}^{N \times L}$ denotes the transmitted pilot symbols and and $[\boldsymbol{G}(\boldsymbol{\theta})]_{k,l} = G_l(\theta_l)$, where $\boldsymbol{\theta} = [\theta_0, \ldots, \theta_{L-1}]^\top$ denotes the RIS phase profile vector. Here, $k = 0, \ldots, N-1$ indexes subcarriers and $l = 0, \ldots, L-1$ indexes OFDM symbols.

B. Channel parameter estimation

The unknown channel parameters are estimated using a two-stage algorithm to reduce complexity. First, we assume the received signal contains only the direct LoS path and estimate its parameters. Then, the residual signal is used to estimate the parameters of the reflected RIS path. To enable separation of LoS and RIS paths components, we adopt a temporally orthogonal RIS phase design as proposed in [11]. Specifically, the RIS phase profiles alternate in polarity across consecutive time slots, following a Hadamard-based structure [18]. This design ensures the received signals exhibit complementary structures across time, which allows path separation via simple slot-wise post-processing. Let $\tilde{\boldsymbol{Y}} \in \mathbb{C}^{N \times L}$ denote the frequency-domain received signal across L time slots. The direct and reflected components are extracted as: $[\tilde{\boldsymbol{Z}}]_l = [\tilde{\boldsymbol{Y}}]_{:,2l} \pm [\tilde{\boldsymbol{Y}}]_{:,2l+1}$, where the index l refers to the slot pair. The sum isolates the direct path ($[\tilde{\boldsymbol{Z}}] = \tilde{\boldsymbol{Z}}_{\mathrm{LoS}}$), while the difference isolates the reflected path ($[\tilde{\boldsymbol{Z}}] = \tilde{\boldsymbol{Z}}_{\mathrm{RIS}}$). This process suppresses inter-path interference and enhances the Signal-to-Noise Ratio (SNR) for parameter estimation. For the LoS path, we correlate the separated signal with a local replica of the model (5) using candidate delay and Doppler values. Since delay affects the rows and Doppler the columns, parameters can be estimated independently via a 2D Fast Fourier Transform (FFT) or two 1D FFTs with non-coherent integration. The resulting coarse estimates are refined using numerical optimization, such as the Newton-Raphson method. Once the LoS contribution is removed from the received signal, the RIS path parameters are estimated similarly. The time-delay is estimated as for the case of the direct path. Once the time-delay is compensated, we correlate the residual signal with RIS steering vectors over grids of candidate Doppler shifts and AoDs. This correlation is efficiently implemented via FFT-based search and optionally followed by a refinement step. More details on the channel parameters estimation algorithm can be found at [11].

C. Position estimation

The UTs' position is estimated using the geometrical channel parameters. First, its direction is determined from the estimated $\hat{\boldsymbol{\theta}}_D$. Then, the UT-RIS distance is estimated by minimizing the cost function $f(d) = \Big(d + \|\boldsymbol{s}_{\mathrm{TR}}\| - \|\boldsymbol{s}_{\mathrm{TR}} - d\mathbf{k}(\hat{\theta}_{\mathbf{D}})\| - \Delta r\Big)^2$, which is derived from the estimated delays $\Delta r = c(\|\hat{\tau}_r - \hat{\tau}_d\|)$. Note that $\boldsymbol{s}_{\mathrm{TR}} = \boldsymbol{p}_{\mathrm{Tx}} - \boldsymbol{p}_{\mathrm{RIS}}$. Finally, the estimated $\hat{\boldsymbol{p}}$ is obtained by scaling the direction vector as $\hat{\boldsymbol{p}} = \widehat{d\mathbf{k}}(\hat{\theta}_{\mathbf{D}})$.

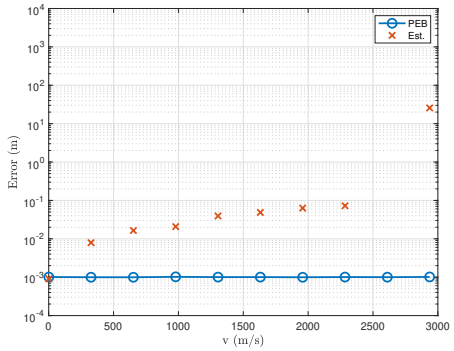

Fig. 3. Position error as a function of the UT velocity, with velocity direction $(-v, v, 0)$, where $v \in [0, v_{\max}]$.

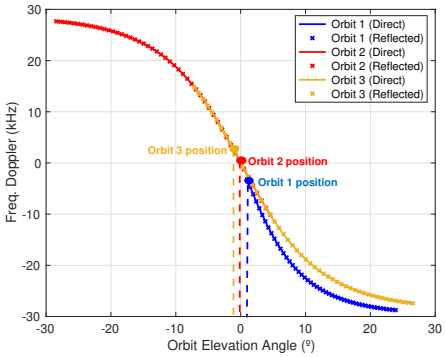

Fig. 4. NTN scenario dynamic: Doppler frequency at reception (LoS and RIS paths) for three orbits across all elevation angles. Highlighted satellite positions: Orbit 1, 2, and 3 with $\psi = \{1, 10^{-4}, -1.5\}^\circ$.

IV. Key performance indicators evaluation

This section evaluates accuracy, dynamic range, and coverage in both TN and NTN systems. We begin by analyzing the estimation algorithm's dynamic range, which is particularly critical in NTN scenarios due to the influence of satellite-induced velocity. Prior studies have shown that under static conditions, where the UT remains stationary, the Cramér-Rao lower bound (CRLB) closely matches the RMSE, validating the estimator's efficiency. We then compare positioning accuracy between TN and NTN under these static conditions to establish a fair performance baseline. Finally, we investigate how satellite motion affects positioning accuracy in NTN by isolating its impact. All results are obtained in Frequency Range 1 (FR1) at 1.432 GHz, using a 60 kHz subcarrier spacing, 1333 subcarriers (corresponding to 80 MHz bandwidth), an 8 dB noise figure, and a 64×64 RIS. Following 3rd Generation Partnership Project (3GPP) [19], the TN scenario uses a transmit power of 20 dBm, while NTN employs 63 dBm with $L = 256$ transmissions. Unless otherwise specified, we assume $\boldsymbol{p}_{\text{BS}} = [5, 5, 0]$, $\boldsymbol{p}_{\text{RIS}} = [0, 0, 0]$, and a directional RIS profile uncertainty of $\sigma = 1$ m.

A. Dynamic range

The dynamic range of the estimation algorithm is evaluated in terms of its ability to maintain position accuracy under varying UT velocities. Accuracy is quantified using RMSE as a function of UT speed. A key metric is the maximum supported velocity, defined as $v_{\max} = \lambda/(4T_{\text{sym}})$, which represents the highest UT speed for which accurate positioning is theoretically achievable. This limit is derived from the maximum tolerable Doppler shift in III-A. The simulator enables the tuning of algorithm parameters to ensure robust localization in dynamic environments. To assess dynamic performance, Monte Carlo simulations at fixed UTpositions while varying the velocity. As shown in Fig. 3, the TN system exhibits position accuracy closely following the CRLB at low velocities, with the RMSE remaining below 10 cm up to approximately 2250 m/s. However, at higher speeds approaching 3000 m/s, the RMSE increases significantly. This degradation stems from inter-carrier interference and reduced separability of LoS and NLoS paths, effects not captured by the CRLB model, leading to increasing discrepancies between the CRLB and actual estimation accuracy at high velocities.

B. Accuracy

1) Cramer-Rao Lower Bound: A fundamental benchmark for accuracy is the CRLB, which provides a theoretical lower bound on estimation errors. First, we determine the CRLB for the unknown channel parameters vector $\boldsymbol{\zeta}_{\text{ch}} \doteq [\tau_d, \tau_r, [\theta_D]_{\text{az}}, [\theta_D]_{\text{el}}, v_d, v_r, \Re(g_d), \Im(g_d), \Re(g_r), \Im(g_r)]^\top$, with g_d and g_r being the channel gain of LoS and RIS paths. This bound is given by $\mathbb{E}(|[\boldsymbol{\zeta}_{\text{ch}}]_m - [\hat{\boldsymbol{\zeta}}_{\text{ch}}]_m|^2) \geq [\mathbf{F}_{\text{ch}}^{-1}]_{m,m}$ with $\boldsymbol{F}_{\text{ch}}$ the FIM of channel parameters [20]. The l-th, k-th element of this matrix $\Lambda(\zeta_l, \zeta_k)$ is given as in [11]. For position estimation accuracy, we consider the positional parameters $\boldsymbol{\zeta}_{\text{po}} \doteq [\boldsymbol{p}, \delta t, v_d, v_r, \Re(g_d), \Im(g_d), \Re(g_r), \Im(g_r)]$ and the FIM given by $\boldsymbol{F}_{\text{po}} = \boldsymbol{J}\boldsymbol{F}_{\text{ch}}\boldsymbol{J}^T$, where $\boldsymbol{J}$ is the Jacobian mapping their relationship. Then, the PEB bounds position estimation error as $\mathbb{E}(|\boldsymbol{p} - \hat{\boldsymbol{p}}|^2) \geq \sqrt{\text{trace}([\boldsymbol{F}_{\text{po}}^{-1}]_{1:3,1:3})}$.

2) TN and NTN systems: In the NTN system, Doppler and range-rate effects are significantly more pronounced than in TN systems, where such impairments are negligible. To assess their impact, three satellite positions are considered: Orbit 1 ($\psi = 1^\circ$), Orbit 2 ($\psi = 10^{-4^\circ}$), and Orbit 3 ($\psi = -1.5^\circ$), as shown in Fig. 4. Results indicate Doppler shifts can reach up to ± 30 kHz and range-rate variations up to ± 90 ms. In Orbits 1 and 3, these effects cause sharp increases in the RMSE, particularly when RIS-induced Doppler approaches 20 kHz, pushing the system toward its performance limits. In contrast, Orbit 2, with negligible Doppler and range-rate, enables the NTN system. Although Doppler in NTN systems is inherently time-varying, it can be approximated as constant over short periods (e.g., L symbols), where it typically remains under 0.1 Hz. Nonetheless, variations in CN0 and AoA across symbols contribute to the dynamic behavior of these systems and affect estimation performance. As illustrated in Fig. 5, for user positions along $[-r/\sqrt{2}, r/\sqrt{2}, -10]$, NTN systems underperform compared to TN systems primarily due to lower CN0 (~ 50 dB). The TN system achieves stable, near-optimal performance, validating the CRLB. The choice of RIS phase profile also influences accuracy. Directional profiles significantly improve performance in low-Doppler scenarios but degrade under high Doppler due to AoD sensitivity. Conversely, random profiles offer more stable performance in dynamic conditions but underperform in ideal ones unless Doppler compensation is applied. Reducing the number of subcarriers further degrades accuracy, especially at large r values with random profiles, where low SNR causes errors to exceed the PEB.

C. Coverage

Coverage is assessed using the PEB computed over user positions $\boldsymbol{p} = [x, y, -5]^T$, with $x \in [-300, 150]$ m and $y \in [10, 500]$ m, to identify sub-meter accuracy regions. For the TN scenario, the base

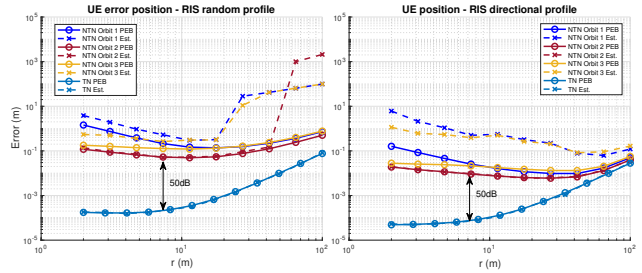

Fig. 5. Estimation error and CRLB for UT position along $[-r/\sqrt{2}, r/\sqrt{2}, -10]$ with $r = [2, 100]$ m, for TN and NTN system.

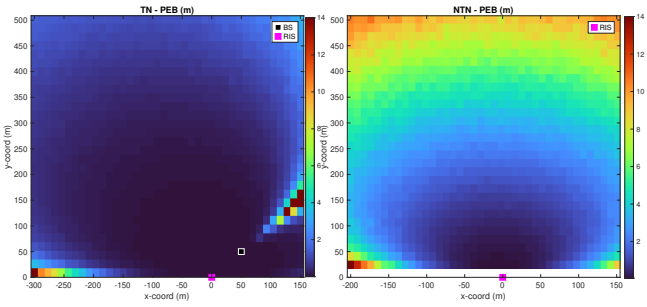

Fig. 6. Coverage analysis for different UT positions using PEB,for TN and NTN system.

station is located at $\boldsymbol{p}_{\mathrm{BS}} = [50, 50, 0]^T$ m, while the NTN system uses a satellite at $\boldsymbol{p}_{\mathrm{sat}} = [-0.8383\mathrm{e}6, 0.8383\mathrm{e}6, 1.1067\mathrm{e}6]^T$ m. In both cases, the RIS is placed at the origin. To isolate motion effects, we analyze coverage at $v = 0$, and use PEB instead of RMSE for computational efficiency. Figure Fig. 6 shows that the TN system achieves sub-meter accuracy in approximately 79% of the area, especially near the RIS and BS, while accuracy degrades beyond 7 m in just 0.83% of the area, particularly in regions behind the BS due to poor geometry diversity and the limited signal paths. Conversely, the NTN system achieves sub-meter accuracy in 13.8% of the area, with positioning errors exceeding 7 m in 18%, mainly due to Doppler and CN0 variations. While higher carrier frequencies reduce coverage in both systems, requiring larger RISs to compensate, the broader footprint of NTN offers potential for improved performance with enhanced RIS designs or better receiver sensitivity. A combined TN-NTN approach could leverage the strengths of both systems for robust, high-accuracy localization across diverse environments.

V. Conclusion

This study evaluated localization performance in both TN and NTN systems, focusing on accuracy, dynamic range, and coverage. TN systems consistently deliver sub-meter accuracy and exhibit strong robustness to mobility, maintaining reliable performance up to velocities of $\sim$ 1500 m/s when operating in FR1 with high bandwidth. In contrast, NTN systems are more susceptible to satellite-induced Doppler and range-rate effects, with performance strongly influenced by orbital geometry. Under favorable conditions, such as Orbit 2 with $\psi = 10^{-4^\circ}$, Doppler effects are minimal, and NTN systems can closely approach the CRLB, achieving accuracy similar to that of TN systems. In terms of coverage, TN systems provide sub-meter accuracy in about 79% of the area. However, this coverage shrinks at higher frequencies (Frequency Range 2 (FR2)) unless larger RISs are used. NTN systems, while more limited in coverage due to CN0 and Doppler variations, still achieve sub-meter accuracy in 18% of the area. They benefit from the satellite's wide footprint and can match TN performance with improved design, such as larger or multiple RISs, optimized waveform settings, or better receiver sensitivity. Overall, TN systems are ideal for high-accuracy localization in low-to-medium velocity scenarios. NTN systems offer wider coverage but require more complex system optimization. A hybrid solution that combines both systems can provide robust and accurate localization across varied environments. Future work should focus on integration strategies and improved algorithms to better handle motion effects in NTN systems.

References

[1] A. Behravan, V. Yajnanarayana, M. F. Keskin, H. Chen *et al.*, "Positioning and sensing in 6G: Gaps, challenges, and opportunities," *IEEE Veh. Technol. Mag.*, vol. 18, no. 1, pp. 40–48, 2022.

[2] W. Saad, M. Bennis, and M. Chen, "A Vision of 6G Wireless Systems: Applications, Trends, Technologies, and Open Research Problems," *IEEE Netw.*, vol. 34, no. 3, pp. 134–142, 2020.

[3] W. Jiang, Q. Zhou, J. He *et al.*, "Terahertz communications and sensing for 6G and beyond: A comprehensive review," *IEEE Commun. Surv. Tutor.*, 2024.

[4] S. Chen and J. Zhao, "The requirements, challenges, and technologies for 5G of terrestrial mobile telecommunication," *IEEE Commun. Mag.*, vol. 52, no. 5, pp. 36–43, 2014.

[5] Z. Li, J. Hu, H. nd Zhang, and J. Zhang, "RIS-Assisted mmWave networks with random blockages: Fewer large RISs or more small RISs?" *IEEE Trans. Wireless Commun.*, vol. 22, no. 2, pp. 986–1000, 2023.

[6] D. Dardari, N. Decarli, A. Guerra, and F. Guidi, "LOS/NLOS near-field localization with a large reconfigurable intelligent surface," *IEEE Trans. Wireless Commun.*, vol. 21, no. 6, pp. 4282–4294, 2021.

[7] M. M. Azari, S. Solanki, S. Chatzinotas, *et al.*, "Evolution of non-terrestrial networks from 5G to 6G: A survey," *IEEE Commun. Surv. Tutor.*, vol. 24, no. 4, pp. 2633–2672, 2022.

[8] L. Wang, P. Zheng, X. Liu *et al.*, "Beamforming design and performance evaluation for RIS-aided localization using LEO satellite signals," in *IEEE ICASSP 2024*. IEEE, 2024, pp. 13 166–13 170.

[9] K. Keykhosravi, M. F. Keskin, S. Dwivedi *et al.*, "Semi-passive 3D positioning of multiple RIS-enabled users," *IEEE Trans. Veh. Technol.*, vol. 70, no. 10, pp. 11 073–11 077, 2021.

[10] D.-R. Emenonye, H. S. Dhillon, and R. M. Buehrer, "Fundamentals of RIS-aided localization in the far-field," *IEEE Trans. Wireless Commun.*, vol. 23, no. 4, pp. 3408–3424, 2023.

[11] K. Keykhosravi, M. F. Keskin, G. Seco-Granados *et al.*, "RIS-Enabled SISO Localization Under User Mobility and Spatial-Wideband Effects," *IEEE J. Sel. Top. Signal Process.*, vol. 16, no. 5, pp. 1125–1140, 2022.

[12] Z. Zhang, L. Dai, X. Chen *et al.*, "Active RIS vs. passive RIS: Which will prevail in 6G?" *IEEE Trans. Commun.*, vol. 71, no. 3, pp. 1707–1725, 2022.

[13] S. Hassouna, M. A. Jamshed, M. Ur-Rehman, M. A. Imran, and Q. H. Abbasi, "Ris-assisted near-field localization using practical phase shift model," *Scientific Reports*, vol. 14, no. 1, p. 4350, 2024.

[14] K. Keykhosravi, M. F. Keskin, G. Seco-Granados *et al.*, "6G RIS-aided single-LEO localization with slow and fast Doppler effects," *arXiv:2410.11010*, 2024.

[15] P. Zheng, X. Liu, J. He *et al.*, "LEO satellite and RIS: Two keys to seamless indoor and outdoor localization," *arXiv:2312.16946*, 2023.

[16] E. D. Kaplan and C. Hegarty, *Understanding GPS/GNSS: principles and applications*. Artech house, 2017.

[17] S. Saleh, M. F. Keskin, B. Priyanto, M. Beale, P. Zheng, T. Y. Al-Naffouri, G. Seco-Granados, and H. Wymeersch, "6g ris-aided single-leo localization with slow and fast doppler effects," in *GLOBECOM*.

[18] K. Keykhosravi and H. Wymeersch, "Multi-RIS discrete-phase encoding for interpath-interference-free channel estimation," *arXiv:2106.07065*, 2021.

[19] 3GPP, "Solutions for NR to support non-terrestrial networks (NTN) (Release 16)," 3GPP, Technical Report TR 38.821, 2021.

[20] S. M. Kay, *Fundamentals of statistical signal processing: estimation theory*. Prentice-Hall, Inc., 1993.